ACS NANO
Cite This: *ACS Nano* XXXX, XXX, XXX−XXX
www.acsnano.org

ARTICLE

Influence of Softness on the Stability of Binary Colloidal Crystals

R. Allen LaCour,[†] Carl Simon Adorf,[†] Julia Dshemuchadse,[†] and Sharon C. Glotzer*,[†,‡,§]

[†]Department of Chemical Engineering, [‡]Department of Materials Science and Engineering, and [§]Biointerfaces Institute, University of Michigan, Ann Arbor, Michigan 48109, United States

Supporting Information

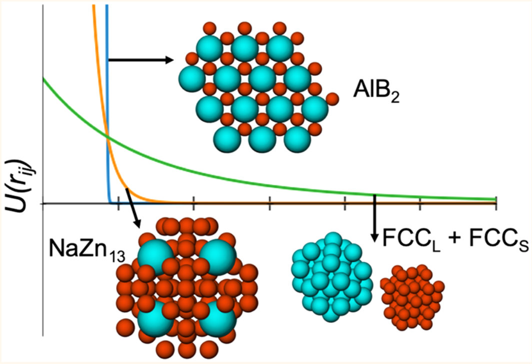

ABSTRACT: **Mixtures of two types of nanoparticles can self-assemble into a wide variety of binary colloidal crystals (also called binary nanoparticle superlattices), which are interesting for their structural diversity and potential applications. Although so-called packing models—which usually treat the particles as "hard" with only excluded volume interactions—seem to explain many reported dense crystalline phases, these models often fail to predict the right structure. Here, we examine the role of soft repulsive interparticle interactions on binary colloidal crystals comprising two sizes of spherical particles; such "softness" can arise due to ligand shells or screened electrostatics. We determine the ground state phase diagram of binary systems of particles interacting with an additive inverse power law potential using a basin hopping algorithm to calculate the enthalpy of an extremely large pool of candidate structures. We find that a surprisingly small amount of softness can destabilize dense packings in favor of less densely packed structures, which provides further evidence that considerations beyond packing are necessary for describing many of the observed phases of binary colloidal crystals. Importantly, we find that several of the phases stabilized by softness, which are characterized by relatively few interparticle contacts and a tendency for local icosahedral order, are more likely to be observed experimentally than those predicted by packing models. We also report a previously unknown dense AB$_4$ phase and conduct free energy calculations to examine how the stability of several crystals will vary with temperature. Our results further our understanding of why particular binary colloidal crystals form and will be useful as a reference for experimentalists working with softly repulsive colloids.**

KEYWORDS: *binary crystals, colloidal crystals, binary nanoparticle superlattices, inverse power law potential, basin hopping*

Binary systems of spheroidal colloids self-assemble into many more colloidal crystal phases than do unary systems of the same particles.[1−6] These phases, which typically have structures analogous to intermetallic or ionic crystals, are interesting for their structural diversity and promising functionalities.[7−11] The particles may differ in composition, charge, size, and shape, each of which influences their self-assembly behavior and potential applications. Models based on hard particle packings are often invoked to explain experimentally observed phases, with varying degrees of success.[6,12−16] Failure of packing models to explain observed phases, in particular, for particles with screened electrostatics[17,18] and/or ligand shells,[6,19] could be due to entropic forces[20] or because the interparticle interaction in those systems is considerably softer than the excluded volume (hard particle) interaction considered by packing models.[21−24] Although the role of entropy has been widely considered,[4,20,25−29] the effect of interaction softness on self-assembled colloidal crystal phases has received less attention,[23,28,30−32] especially for binary systems.

Here, we examine the enthalpic influence of softness on the colloidal crystal phase behavior of binary mixtures of spherical particles of two different sizes interacting *via* an additive inverse power law (IPL) potential. We investigate a much wider range of softness than has been reported to date by tuning the exponent of the IPL to vary the distance over which the repulsive interaction falls off from the surface of a particle. Large exponents describe a very rapid decay (and thus "harder" interparticle interaction), whereas small exponents describe a slow decay (becoming a $1/r$ decay with an exponent of one). To isolate the role of softness from other effects, we perform zero-temperature enthalpy calculations (which disregard entropy) to determine the ground state stability of different phases. We find several experimentally observed phases that fail to be described by packing models; instead, we show that these phases, which have a small number of interparticle

Received: June 1, 2019
Accepted: November 6, 2019
Published: November 6, 2019

DOI: 10.1021/acsnano.9b04274
ACS Nano XXXX, XXX, XXX−XXX

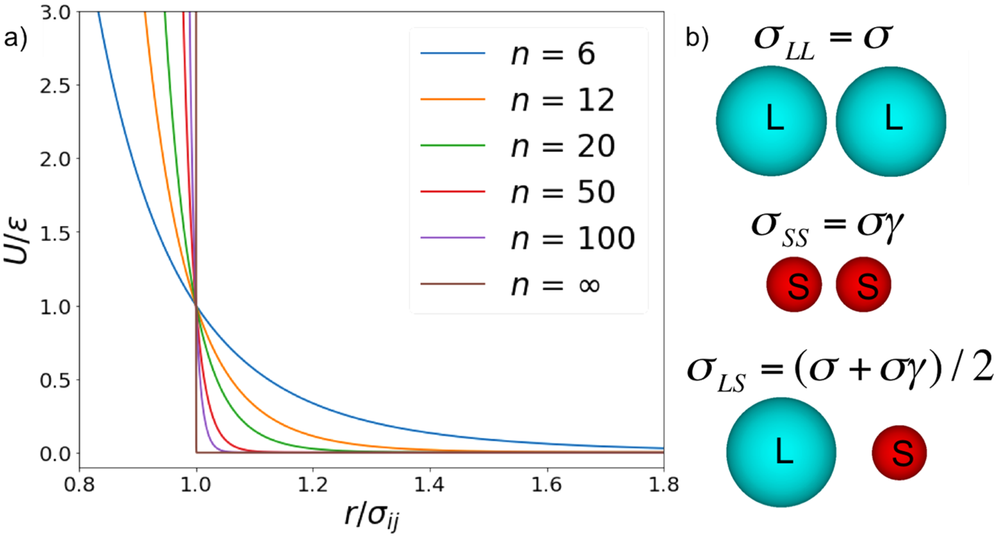

Figure 1. (a) Plots of the IPL model for different values of n and (b) effective size of different types of particles. The pair potential is given by eq 1 and is plotted over r/σ_{ij}—the distance between two particles i and j divided by the average size of the particles. The large and small particles are represented by "L" and "S", respectively. The quantity σ is the size of the large particles, and γ is the size ratio between the small and large particles. Unlike particles interact as though they are the average size of the two particles.

contacts and a tendency for icosahedral local order, are stabilized by particle softness. We also use finite temperature free energy calculations to probe the influence of temperature for a few phases, generally finding agreement with our ground state calculations with the exception of a recently reported dense packing phase.[33] We further find that a small amount of softness (described by a very large IPL exponent) can influence phase behavior away from that describable by packing models. These deviations from hard sphere packing behavior partially explain why the packing fractions of different phases do not solely determine their self-assembly behavior, as is commonly invoked. We characterize the degree of softness necessary to destabilize any binary phases relative to phase-separated unary phases for the additive IPL potential, which has relevance for the modeling of binary systems and our understanding of the interaction between different species of particles. Finally, we relate our results to recent experimental reports, elucidating how repulsive forces contribute to the formation of particular structures observed in experiments.

Model. The use of packing models to understand the behavior of condensed phases stems in part from the ground state of the hard sphere model, in which particles are prohibited from overlapping; the ground state is the phase with the highest packing fraction at infinite pressure. Throughout this work, we use the term ϕ_m to describe the maximum packing fraction obtainable by hard spheres in a particular structure. The binary hard sphere model, in which the particles can be one of two different sizes, describes the phase behavior of many binary colloidal systems, as shown by free energy calculations.[25,28,34,35] However, no real particle is perfectly hard,[21,22] and in many cases—particularly the self-assembly of metal and semiconductor nanoparticles—experimental results differ from binary hard sphere predictions.[3−5,18,36]

In contrast to hard particle models, softly repulsive pair potentials in binary systems have received much less consideration. In 2009, Hynninen *et al.* found the CsCl and Laves phases to be stable for a particular binary Yukawa potential.[28] In 2015 and 2016, Travesset and Horst found several more binary phases to be stable for a binary IPL model.[23,32] However, the Laves phases were the only binary structures found to be stable when the potential was additive (where unlike particles interact as though their size is the average of the two particles); observing other phases required reducing the repulsion between unlike particles. Here, we ascertain how softness affects crystal stability by considering a much wider range of softness.

We studied the IPL potential in eq 1; its parametrization for binary systems is shown in Figure 1.

$$U_{ij} = \epsilon\left(\frac{\sigma_{ij}}{r_{ij}}\right)^n \qquad (1)$$

The quantity n is related to the hardness of the particles, σ_{ij} governs their size, and ϵ determines the units of energy. The quantity γ in Figure 1 gives the size ratio between large and small particles. The potential is specified to be additive as is physically accurate in the limit of n approaching ∞. For $n = \infty$, we obtain the binary hard sphere model; for $n = 1$, we obtain the potential describing Coulombic repulsion.

The phase behavior of our model depends upon n, γ, the stoichiometry, and a variable incorporating both the pressure and temperature. Note that, for the IPL model, giving ϵ as ϵ_{ij} to depend on the types of particles interacting does not increase the generality of the potential as any variation in ϵ_{ij} can also be accounted for through variation in σ_{ij}. The ability to write the temperature and pressure of the IPL model as one variable results from the its thermodynamic scaling properties and is not possible for most pair potentials.[30] We review these scaling properties in section S2.1 of the Supporting Information. By constraining $T = 0$, we are then left with the aforementioned three parameters: n, γ, and the stoichiometry of the system. We will present two slices of the model's phase diagram at constant stoichiometry and four slices at constant n.

We analyze the phase behavior of our potential at constant pressure because the stability of densely packed phases for hard spheres at higher pressures can be justified on the basis of enthalpy alone. The stability of these phases is often

DOI: 10.1021/acsnano.9b04274

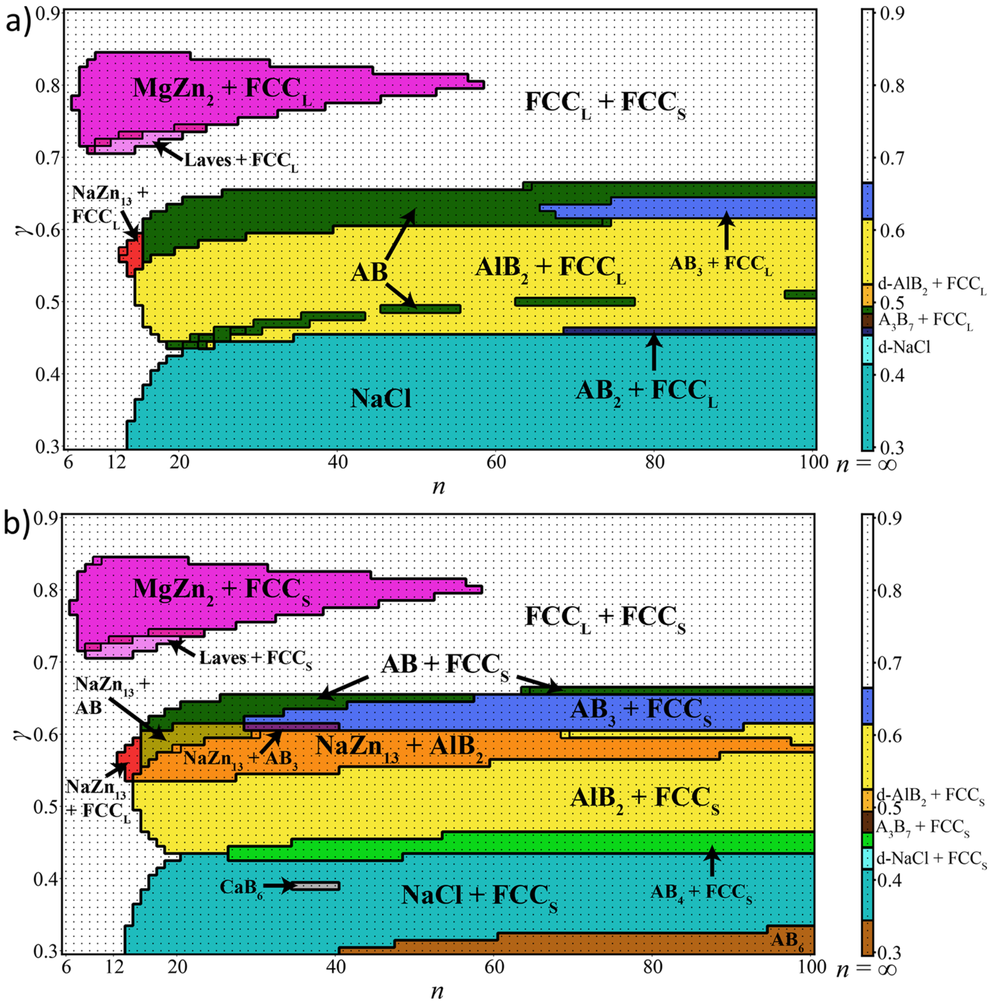

Figure 2. Phase diagrams calculated at stoichiometries of (a) $x_s = 1/2$ and (b) $x_s = 6/7$ for the binary IPL model. The diagrams are given in terms of particle size ratio γ and hardness n. We show 95 values of n spanning from 6 to 100, and 61 values of γ spanning from 0.3 to 0.9. The $n = \infty$ slice to the right of each plot was calculated from the densest packings. The equilibrium state consists of two phases unless the stoichiometry of a phase is identical to that of the system (*e.g.*, CaB$_6$ for $x_s = 6/7$); the colors indicate a region corresponding to a specific set of equilibrium phases. In regions denoted "Laves + FCC$_S$", the differences in enthalpy between the different Laves phases were very small. If the difference in enthalpy between two phases was <0.001%, the point was colored to indicate the presence of the phase nearest in stoichiometry to that of the entire phase diagram. In every region containing "NaCl", the difference in enthalpies between NaCl and NiAs was also <0.001%. The black dots indicate points at which basin hopping runs were performed.

understood in terms of free volume theory, according to which particles in the densest packing phases will have more volume available to them than in other arrangements and thus be entropically favored. However, at constant pressure, the Gibbs free energy in the limit of either zero temperature or infinite pressure can be written as

$$\lim_{P\to\infty} G = \lim_{T\to 0} G = PV \tag{2}$$

Note that the equivalence of these two limits follows directly from the well-known thermodynamic scaling ($P\sigma^3/kT$) between pressure and temperature in hard particle systems (see section S2.1 of the Supporting Information for more details). Densely packed phases will minimize V, motivating the idea that they are the ground states of the system. For completeness, we give two more rigorous proofs that the densest packing phase has minimal free energy in the limit of zero temperature at finite pressure in our Supporting Information; in section S1.5, we take the limit of infinite n in our equation for the enthalpy of soft spheres, and in section S2.2, we take the zero temperature limit of our NPT partition function. Thus, we should expect (and do observe) that densely packed phases will arise in constant pressure ground state calculations of the enthalpy for our potential as n approaches ∞.

The IPL model exhibits thermodynamic scaling of the form $\frac{P\sigma^3}{\epsilon}/\left(\frac{kT}{\epsilon}\right)^{(3/n+1)}$.[37] Note that as n approaches ∞, the scaling reduces to that of hard spheres, and that the $P \to \infty$ behavior is equivalent to that of $T \to 0$. Likewise, one would expect the specific value of the pressure to not affect phase behavior at $T \to 0$ because the scaling term diverges in that limit regardless of P. Indeed, we find this in our derivation of an equation for $H(T = 0, P)$ in the first section of the Supporting Information.

Although the IPL model does not perfectly describe colloidal interactions, we believe it is sufficiently general to account for the behavior of many colloids. In fact, the effective n for several colloidal polymer particles have been previously estimated[21,22,38] and are often similar to the values of n we investigate. In other binary self-assembly experiments, the

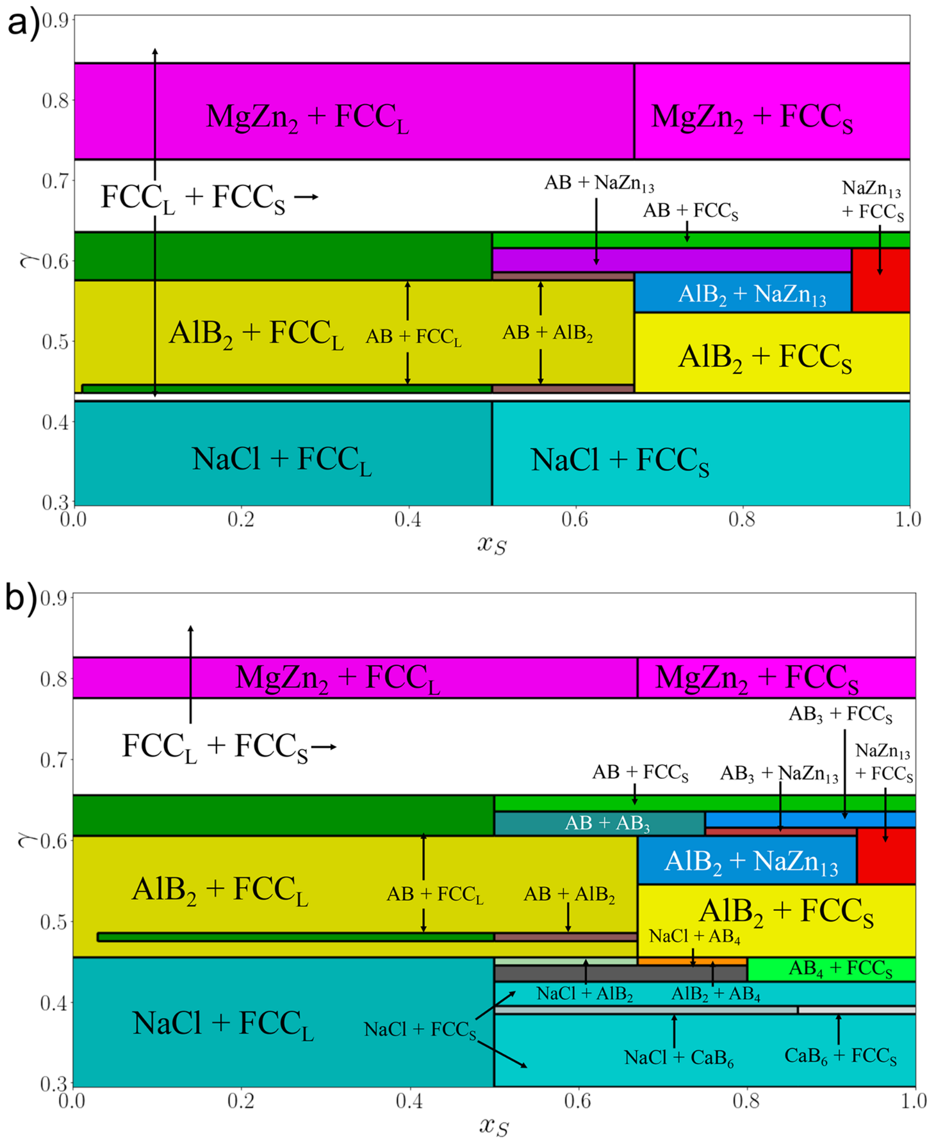

Figure 3. Phase diagrams calculated at n of (a) 20 and (b) 40 for the binary IPL model. The diagrams are given in terms of particle size ratio γ and concentration of small particles, x_s. We use a resolution of 0.01 in determining the phase boundaries with respect to both γ and x_s. The difference in enthalpy between the equilibrium phases and competing combinations of phases is generally >0.001%, with the only exceptions being the differences between $MgZn_2$ and the other Laves phases, the difference between $AB + FCC_L$ and $AlB_2 + FCC_L$ at $\gamma = 0.48$, and the difference between any region containing NaCl and an equivalent region containing NiAs instead.

nature of the interparticle forces during self-assembly is less clear,[39] but similarities between the self-assembled structures formed from many metal and semiconductor nanoparticles and those formed with other softly repulsive particles suggest that repulsive forces play a key role in their assembly, as well. Likely the most notable way in which our model deviates from other notions of softness is our neglect of 3-body interactions, such as the deformation of two particles in contact influencing the way they act with a third particle (which has been implicated as important for understanding the self-assembly of certain ligand-functionalized nanoparticles[6]). Many colloidal particles, such as those in charge-stabilized or hard sphere-like colloids, will be less deformable and thus more likely to correspond to our model.

Travesset and Horst previously investigated the binary IPL potential at $n = 12$ and $n = 6$, while varying the additivity of the potential.[23,32] Here, we investigate n at values from 6 to 100, a range inclusive of many experimental particles, as shown in a recent analysis by Royall *et al.*[22] We keep our potential additive to maintain correspondence with the hard sphere limit.

RESULTS AND DISCUSSION

In Figure 2, we present phase diagrams calculated at stoichiometries of $x_s = 1/2$ and $x_s = 6/7$ in terms of γ and n. Due to the thermodynamic scaling properties of the IPL model, its ground state phase diagram also corresponds to its infinite pressure phase diagram and exhibits no pressure dependence (see section S1.4 of the Supporting Information for more details). We did not evaluate the enthalpy of any dense unary sphere packings other than the face-centered cubic (FCC) crystal due to their great structural similarities (*i.e.*, consisting of hexagonal layers stacked upon each other); we expect them all to have practically identical enthalpies at most n examined. Visualizations of several stable structures without equivalents in the Inorganic Crystal Structure Database[40]

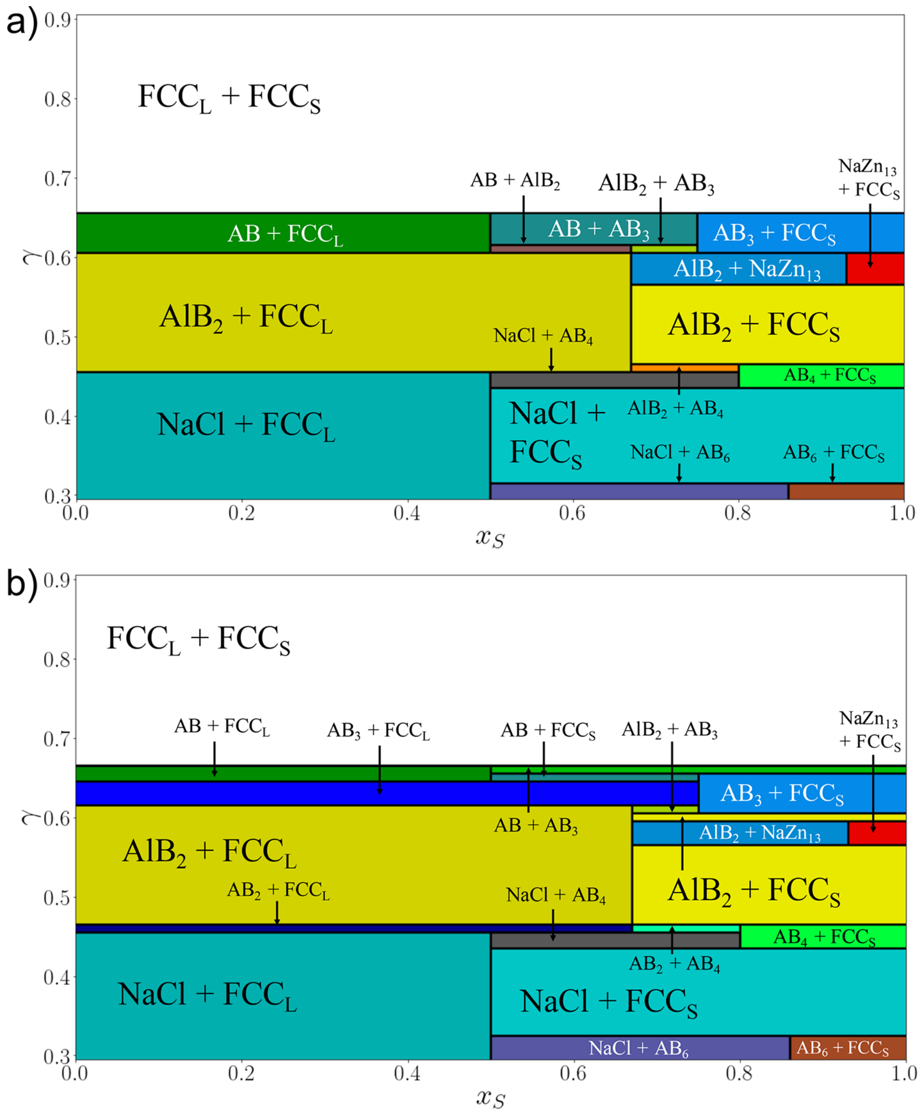

Figure 4. Phase diagrams calculated at *n* of (a) 60 and (b) 80 for the binary IPL model. The diagrams are given in terms of particle size ratio γ and concentration of small particles, x_s. The difference in enthalpy between the equilibrium phases and competing combinations of phases is generally >0.001%, with the only exception being the difference between any region containing NaCl and an equivalent region containing NiAs instead.

(ICSD) are included in section S3 of the Supporting Information.

Regions of phase stability were calculated by finding the combination of phases that minimizes the enthalpy for a given stoichiometry. Unless the stoichiometry of a phase matches the system's stoichiometry (*e.g.*, NaCl for $x_s = 1/2$), the enthalpy at each point in the phase diagram is minimized by two phases: one with a stoichiometry greater than that of the system and one with a stoichiometry less than that of the system. Phases are taken to be in the thermodynamic limit, and thus no attempt was made to account for interfaces between coexisting phases. The specific enthalpy for coexisting phases *a* and *b* was calculated from the standard thermodynamic formula as $x_aH_a + x_bH_b$, where x_a and x_b are determined through application of the lever rule to the natural stoichiometry of each phase *a* and *b* and the global stoichiometry of the system. We examined every possible combination of our candidate phases to determine the pair with the lowest enthalpy.

The phases present at $n = \infty$ correspond to the most densely packed combination of phases at the particular γ and stoichiometry obtainable with our set of candidate structures. With the exception of a densely packed phase we discovered, we generated the $n = \infty$ regions from the work of Hopkins *et al.*[41,42] and Filion *et al.*,[43] who both analyzed the densest packings of binary sphere systems. We denote structures with no clear atomic counterpart by A_xB_y, with *x* and *y* giving the stoichiometry. Certain structures that appear on Hopkins *et al.*'s phase diagram fail to appear on ours because the region of size ratios over which they are the densest packing is smaller than the resolution of our phase diagram (0.01), but we still examined the stability of these phases for finite *n* at the size ratios we did investigate. AB_4 is the aforementioned phase discovered to be a densely packed phase over the course of this work. The regions denoted d-NaCl and d-AlB_2 contain versions of NaCl or AlB_2 slightly distorted from their cubic or hexagonal symmetry into orthorhombic or monoclinic crystals, respectively, to have larger ϕ_m. Densest packing structures are also common at $n = 100$. A notable exception is A_3B_7 (a slightly symmetrized version of a structure reported by

Hopkins *et al.*[42]), which is not present for $n \leq 100$, despite being the densest packing for $\gamma = 0.47$.

For $n \leq 100$, we found 11 equilibrium phases. Seven of these correspond to experimentally observed phases:[1−6,44] FCC, NaCl, AlB_2, $MgZn_2$, AB_4, CaB_6, and $NaZn_{13}$. The four remaining phases are known to pack very densely.[41,42,45] AB_6 is a distorted version (from cubic to orthorhombic) of the bcc-AB_6 phase observed experimentally.[46] AB_2 is an orthorhombic phase with space group symmetry $Cmc2_1$ (no. 36). AB is an orthorhombic phase with space group symmetry *Pmnc* (no. 62) and is particularly interesting for the high γ at which it appears. AB_3 is an orthorhombic phase with space group symmetry *Pmmn* (no. 59).

In general, lower symmetry sets of space groups and Wyckoff sites are capable of producing multiple distinct structures through variation of their degrees of freedom. For example, a structure in space group *Pmnc* (no. 62) with both the large and small particles in Wyckoff sites, 4*c* will become the much higher symmetry structure NaCl for particular values of the free parameters and can be converted into several other densely packed structures for other values;[45] slight variations in the values will produce slightly distorted structures. In this manner, our basin hopping procedure enabled us to search thousands of structures, including slightly distorted versions of common structures like NaCl. Thus, while it is likely that we missed some structures, we think enlarging our search space will not significantly alter the conclusions drawn in this paper.

Variable Stoichiometry Phase Diagrams. In Figures 3 and 4, we plot phase diagrams at constant n but variable stoichiometry and particle size ratio. The values of n considered are 20, 40, 60, and 80. These phase diagrams were generated in a manner similar to those in Figure 2: discrete values of the parameters were selected, and the combination of phases resulting in the minimum enthalpy for those values was determined by comparing all possible combinations. Because we only consider the possibility of crystals of constant stoichiometry (as opposed to liquids and solid solutions), every region will contain two phases bounded by the x_s of the phases present within the region. However, we observe deviations from this for the AB + FCC_L region of our phase diagrams in Figure 3, whose enthalpy is extremely similar to that of the AlB_2 + FCC_L region; we note that these deviations do not represent any thermodynamic anomaly but are instead related to our lack of confidence in accurately distinguishing the difference in enthalpy between the two phases.

Although Figures 3 and 4 contain only phases present in Figure 2 (we chose the slices in Figure 2 such that they would contain at least a small region of every phase we found to be stable), we plot them to more clearly illustrate the influence of stoichiometry and to inspire experimentalists to test our predictions. Of course, these thermodynamic calculations will not account for experiments involving nonequilibrium phenomena or polydispersity, such as the assembly of more than three different superlattices from a single batch of nanoparticles[5] or heterogeneous effects, like the formation of wetting layers between different superlattices,[44] but should be a guide for the behavior of such particles under certain ideal conditions.

Influence of Temperature. An immediate concern for our phase diagram is how well our our ground state calculations reproduce actual assembly behavior at finite temperatures. Ideally, we could use direct self-assembly simulations to determine the phase behavior of our systems, in which we cool down a simulation of the fluid until we observe nucleation of the solids. Such methods provide relatively unambiguous determination of the preferred solid configuration of a particular set of particles, eliminating the need to examine the stability of other solids. However, in binary systems of mutually repulsive particles, the slow assembly kinetics often render such simulations computationally infeasible.[47−49] This is less of an issue for experiment, in which the time scales and number of particles are typically orders of magnitude larger than currently possible with computation. This difficulty has resulted in equilibrium calculations[25,28,34,35] providing much of our basic understanding of self-assembly in such systems. We do note two recent papers where binary assembly was observed for mutually repulsive particles by using specialized Monte Carlo techniques with particle swaps[49] or, intriguingly, tuning the softness of the particles.[50] We discuss possible influences of kinetics on self-assembly structure in the Experimental Relevance section.

More tractable is the issue of how increasing the temperature changes the relative free energies of different structures. Whereas the ground state phase is often predictive of finite temperature behavior, several cases exist in the literature in which raising temperature changes the preferred solid structure.[51,52] As self-assembly generally occurs at higher temperatures, and large energy barriers may prevent solid−solid phase transitions at low temperature, finite temperature free energies should be more predictive of actual behavior.

In Table 1, we present the absolute Gibbs free energies of several structures for five points in our phase diagram, computed from a variant of the Frenkel−Ladd method.[53,54] We focus on less hard n between 12 and 40, where we see several experimental structures on our phase diagram. We examined G at a range of pressures using thermodynamic integration of pressure−volume data but present it only for the lowest pressure (least supercooled) in Table 1. We note that our calculations are unable to account for phase behavior all the way to the fluid−solid coexistence due to the lack of a

Table 1. Free Energies of Different Structures at $kT/\epsilon = 1$, $x_s = 6/7$

γ	n	$P\sigma^3/kT$	structures	G/kT	ground state?
0.39	35	203	CaB_6	38.729(15)	yes
0.39	35	203	NaCl + FCC_S	38.806(2)	no
0.39	35	203	FCC_L + FCC_S	39.601(1)	no
0.39	35	203	bcc-AB_6	39.924(4)	no
0.43	40	151	AB_4 + FCC_S	33.673(3)	yes
0.43	40	151	AlB_2 + FCC_S	33.878(3)	no
0.43	40	151	NaCl + FCC_S	33.906(3)	no
0.43	40	151	FCC_L + FCC_S	34.264(4)	no
0.6	20	56	AB + $NaZn_{13}$	23.828(2)	yes
0.6	20	56	FCC_L + $NaZn_{13}$	23.850(1)	no
0.6	20	56	$CaCu_5$ + $NaZn_{13}$	23.893(3)	no
0.6	20	56	AB_3 + $NaZn_{13}$	24.084(2)	no
0.63	40	48	AB + FCC_S	22.445(3)	no
0.63	40	48	FCC_L + FCC_S	22.489(4)	no
0.63	40	48	$CaCu_5$ + FCC_S	22.491(3)	no
0.63	40	48	AB_3 + FCC_S	22.527(4)	yes
0.63	40	48	FCC_L + $NaZn_{13}$	22.5363(1)	no
0.81	12	31	$MgZn_2$ + FCC_S	24.108(5)	yes
0.81	12	31	FCC_L + FCC_S	24.159(3)	no

comprehensive equation of state for the binary IPL fluid; instead, we were limited by the melting point of an FCC crystal of the small particles.[55] These points were chosen to test the stability of more unusual structures at finite temperatures. $CaCu_5$ and bcc-AB_6 are the only two structures not mentioned previously; their symmetry and Wyckoff sites are given in Table 2. The values in parentheses correspond to the standard deviation × 10^3 across three independent sets of simulations.

Table 2. Candidate Structure Types

			Wyckoff sites	
structure type	space group		L	S
*cF*8-NaCl	$Fm\bar{3}m$	225	4*a*	4*b*
*hP*4-NiAs	$P6_3/mmc$	194	2*a*	2*c*
*cP*2-CsCl	$Pm\bar{3}m$	221	1*a*	1*b*
*tP*2-CuAu	$P4/mmm$	123	1*a*	1*d*
*oP*8-AB	$Pnma$	62	4*c*	4*c*
*oC*8	$Cmmm$	65	4*g*	4*j*
*hP*3-AlB_2	$P6/mmm$	191	1*a*	2*d*
*hP*12-$MgZn_2$	$P6_3/mmc$	194	4*f*	2*a*, 6*h*
*hP*24-$MgNi_2$	$P6_3/mmc$	194	4*e*, 4*f*	4*f*, 6*g*, 6*h*
*cF*24-$MgCu_2$	$Fd\bar{3}m$	227	8*b*	16*c*
*oP*12	$P2_12_12_1$	19	4*a*	4*a*, 4*a*
*mC*6	$C2/m$	12	2*a*	4*i*
*oC*12-AB_2	$Cmc2_1$	36	4*a*	4*a*, 4*a*
*hP*6	$P6_3/mmc$	194	2*b*	4*f*
*oP*12	$Pnma$	62	4*c*	4*c*, 4*c*
*mC*12	Cm	8	2*a*, 2*a*	2*a*, 2*a*, 2*a*, 2*a*
*oC*20-A_3B_7	$I222$	23	2*a*, 4*j*	2*c*, 4*j*, 8*k*
*mC*14	Cm	8	2*a*, 2*a*	2*a*, 2*a*, 2*a*, 4*b*
*cP*4-Cu_3Au	$Pm\bar{3}m$	221	1*a*	3*c*
*cF*16-Li_3Bi	$Fm\bar{3}m$	225	4*a*	4*b*, 8*c*
*cP*8-Cr_3Si	$Pm\bar{3}n$	223	2*a*	6*c*
*oC*16	$Cmcm$	63	4*c*	4*c*, 8*g*
*oP*8-AB_3	$Pmmn$	59	2*a*	2*b*, 4*f*
*oF*20	$F222$	22	4*a*	16*k*
*cP*5-Fe_4C	$P\bar{4}3m$	215	1*a*	4*e*
*tP*20-AB_4	$P4bm$	100	4*c*	4*c*, 2*a*, 2*a*, 8*d*
*hP*30	$P6_3mc$	186	6*c*	6*c*, 6*c*, 6*c*, 2*a*, 2*b*, 2*b*
*hP*6-$CaCu_5$	$P6/mmm$	191	1*a*	2*c*, 3*g*
*cP*7-CaB_6	$Pm\bar{3}m$	221	1*a*	6*f*
*cI*14-bcc-AB_6	$\mathrm{Im}\bar{3}m$	229	2*a*	12*d*
*oI*14-AB_6	$Immm$	71	2*a*	4*f*, 4*h*, 4*j*
*cF*112-$NaZn_{13}$	$Fm\bar{3}c$	226	8*a*	8*b*, 96*i*
*cP*14	$Pm\bar{3}m$	221	1*a*	1*b*, 12*i*

The most stable structures are generally in line with those for the ground states, with a deviation only being observed in once case. For $n = 40$ and $\gamma = 0.6$, AB_3 changes from being the ground state to being less favorable than multiple other structures at finite temperatures, which we discuss in our Experimental Relevance subsection. Our free energy calculations also provide evidence that temperature will not destabilize the AB, AB_4, and CaB_6 phases.

Naturally, we expect our phase diagram to be most relevant for systems under high pressure and low temperature. From literature results on the free energies of binary hard sphere systems, we can anticipate other changes to our phase diagram at high temperatures. In particular, we would expect the region over which the Laves phases are stable to extend all the way to $n = \infty$ but over less size ratios at higher n.[28] We also expect that $NaZn_{13}$ would be present all the way to $n = \infty$.[25] Systematically mapping out their (and the other phases') region of stability would require a comprehensive equation of state for the binary IPL fluid.

Minimization of Contacts. The variation in phase stability with n and γ shown in Figure 2 necessarily results from the local environments of each type of particle in the structure. Considering that our pair potential is purely repulsive, low energy (ground state) structures would seem to be those that minimize the number of contacts between particles. However, at $n = \infty$, the densest packing structure becomes favored regardless of the number of interparticle contacts, so ϕ_m obviously plays a role, as well (despite not being directly involved in our calculations), and we find the structures stabilized by softness to have both high ϕ_m and a low number of contacts. The importance of having a high ϕ_m for soft particles comes from its correspondence with the nearest interparticle distance. When comparing two structures at constant number density, the nearest contact distance (defined here as the distance between two particles divided by the average diameter of the particles, σ_{ij}) of the densest packing structure will be largest for the structure with the greater ϕ_m. The nearest contact will be the largest contribution to the energy of the structure; thus higher ϕ_m structures tend to have lower energy than competing phases. This leads to FCC being the stable unary phase for all n examined. The binary phase diagram is more diverse because there are many structures with both high ϕ_m and few contacts. Here, we analyze how having a small number of contacts stabilizes two phases commonly observed in experiment:[1−3,6] AlB_2 and $NaZn_{13}$. In Figure 5, we highlight the structure of AlB_2 optimized for $n = 45$ and $\gamma = 0.46$.

AlB_2 is the densest known packing for $0.53 < \gamma < 0.62$.[42] Its large particles are arranged in simple hexagonal layers whose interstitial voids are occupied by the small particles. The c/a ratio is the only degree of freedom of its unit cell; optimal c/a ratios for particular n and γ and interparticle distances are shown in Figure 5. These distances are scaled by σ_{ij}, the quantity relevant for the IPL potential and for ϕ_m calculations.

Lowering n from ∞ can expand the region of stability for AlB_2 down to $\gamma = 0.43$ despite it packing significantly less effectively than competing phases. For example, the AlB_2 structure reported in Figure 5 is more stable than AB_4 despite AB_4 having a higher ϕ_m (0.759 *vs* 0.722). We can use their ϕ_m values to estimate energy differences, as the cube of the ratio of two structures' nearest contact distances is proportional to the ratio of their ϕ_m values if they have the same stoichiometry (see section S1.5 of the Supporting Information). Therefore, this difference in ϕ_m indicates that the nearest contact of AB_4 (scaled to account for the stoichiometry difference) is $(0.759/0.722)^{1/3} = 1.018$ times farther away than in AlB_2, which, at $n = 45$, corresponds to AlB_2 having $1.018^{45} = 2.12$ times more energy per nearest contact. To define an "average" number of nearest neighbors, we note from Figure 5 that the nearest contact is at a scaled distance of ~1.51. The large particle has 8 such contacts, and the two small particles have none; thus we can define the average number of nearest contacts as 8/3— 2.67. The definition is reasonable as contacts from both large and small particles contribute equally to the total energy. The competing AB_4 structure has ~9.4 nearest contacts (data not shown); this difference enables the less densely packed AlB_2 structure to have a lower energy than AB_4 at $n = 45$. Non-nearest neighbors will also contribute to the total energy of

DOI: 10.1021/acsnano.9b04274

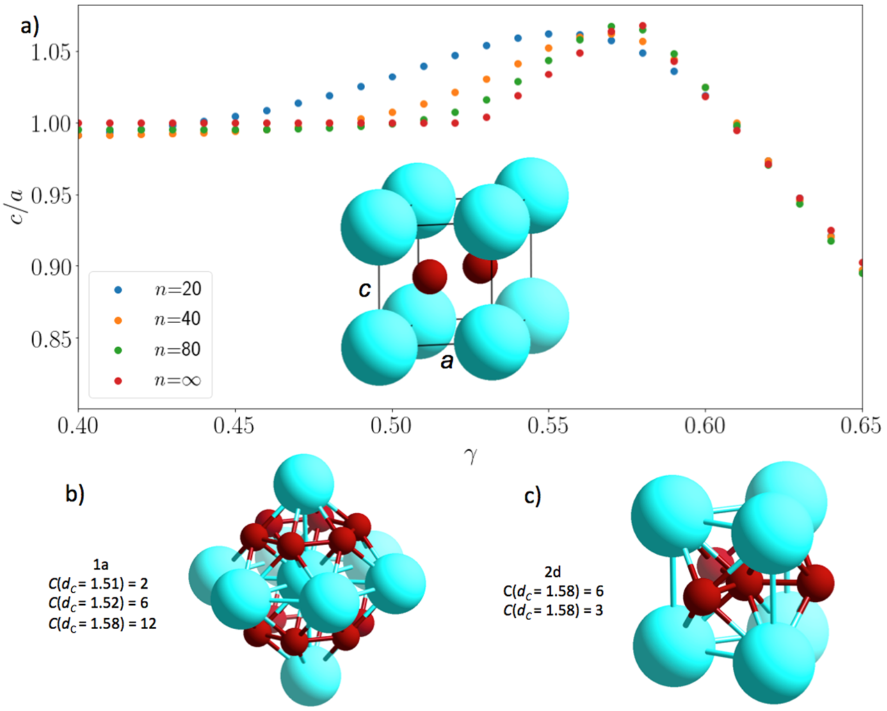

Figure 5. (a) Optimal unit cell parameters (c and a) and local arrangements at the (b) 1a (blue) and (c) 2d Wyckoff sites (red) of the AlB_2 structure. The inset in (a) shows the unit cell of AlB_2 for a $c/a = 1$. This particular AlB_2 structure was optimized for minimal enthalpy at $n = 45$ and $\gamma = 0.46$. C gives the number of particles at a particular contact distance, whereas d_c gives the distance to that particular set of neighbors divided by the average diameter of the particles, *i.e.*, the distance used in the IPL potential. Distances are all calculated with a number density of $1/\sigma^3$.

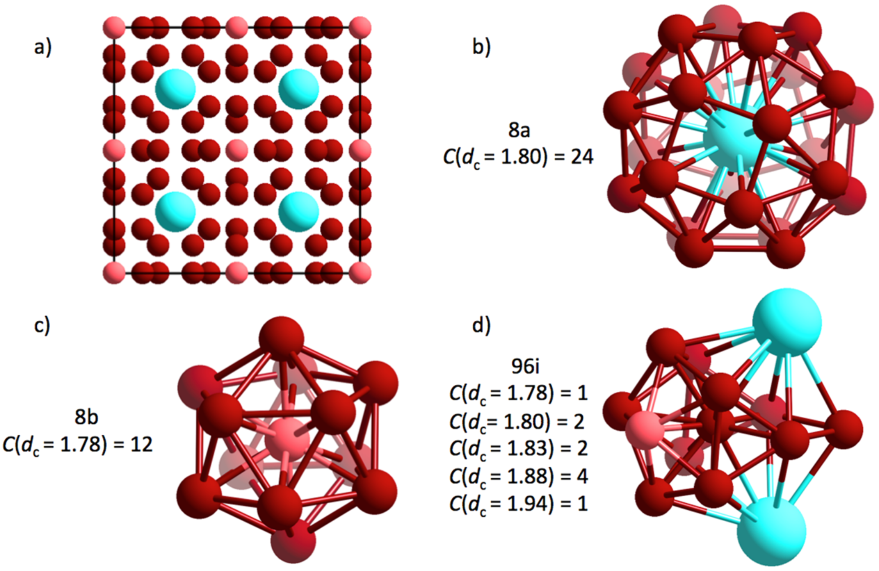

Figure 6. (a) $NaZn_{13}$ unit cell and the environments of its (b) 8a (blue), (c) 8b (light red), and (d) 96i Wyckoff sites (dark red). This particular $NaZn_{13}$ structure was optimized for low enthalpy at $n = 60$ and $\gamma = 0.57$. C gives the number of particles at a particular contact distance, whereas d_c gives the distance to that particular set of neighbors divided by the average diameter of the particles (the distance used in the IPL potential). The distances are all calculated with a number density of $1/\sigma^3$.

both crystals but have a substantially lesser influence than the nearest neighbor.

In $NaZn_{13}$ and several other structures, particles in a few Wyckoff sites have many nearest neighbors, but the average number per particle is low. The local environments of each Wyckoff site in $NaZn_{13}$ are shown in Figure 6. The standard unit cell of $NaZn_{13}$ contains 8 large particles and 104 small particles. Each large particle is surrounded by 24 small particles arranged at the vertices of a snub cube. Small particles in the 8b Wyckoff site occupy the center of an icosahedron of small particles, whereas those in the 96i position occupy the icosahedron's vertices. In general, the snub cube and icosahedron are slightly distorted from the perfect shapes. Despite $NaZn_{13}$'s structural complexity, it is the most commonly observed binary structure in many colloidal self-assembly experiments, occurring across a wide range of particle compositions.[2,6,18]

Particles in the 8*a* (snub cube-coordinated) and 8*b* (icosahedrally coordinated) Wyckoff sites in $NaZn_{13}$ both have nearest neighbors slightly closer than competing structures (*e.g.*, AlB_2); furthermore, they both have a significant number of neighbors at the nearest contact distance. On the other hand, the 96*i* Wyckoff site, which accounts for 6/7 of the total number of particles, has relatively few nearest neighbors, so the average number of nearest neighbors per particle is low. Thus, if the particles are softer, diminishing slightly the relevance of the first contact relative to further neighbors, $NaZn_{13}$ is stable for several values of γ.

It is interesting to consider $NaZn_{13}$'s stability in light of its coordination polyhedron. Both the icosahedron and snub cube are solutions to the Tammes problem, that is, maximizing the smallest interparticle distance constrained on the surface of a sphere.[56,57] Although these distances do not correspond to the nearest contacts in $NaZn_{13}$, they influence the energy for finite n. Due to their distance-maximizing nature, the occurrence of these coordination polyhedra in structures in our phase diagram seems natural.

We suspect that this partially accounts for the icosahedral order observed in many binary nanoparticles superlattices,[58] several of which[11] adopt the structures in our phase diagram. Particularly notable is $MgZn_2$, which, being a Frank-Kasper phase, exhibits a significant amount of icosahedral local arrangements; we also find it to be stable over a substantial region of our phase diagram.

High *n* Limit. In Figure 2, we see that the hard sphere limit is not yet reached for $n = 100$, although the γ values where particular phases are stable do appear to be converging to the hard sphere case. This result is surprising to us, as other studies indicate that, for certain system properties (*e.g.*, melting points, transport coefficients) in unary systems, the hard sphere limit may be effectively reached for $n = 72$ or even $n = 18$.[59,60] To better understand the hard sphere limit, we analyzed the degree to which having few nearest neighbors enhances the stability of a structure.

If n is sufficiently large, the energy of a structure can be approximated as

$$E/N = C\epsilon\left(\frac{\sigma_1}{r_1}\right)^n \tag{3}$$

where C equals the average number of nearest contacts per particle and r_1/σ_1 is the nearest contact distance in the structure. Thus, as mentioned earlier, a structure with low C may be stabilized over other structures with larger nearest contact distances (or, equivalently, larger ϕ_m). By equating the energy of two structures with different C, we can calculate the differences in nearest contact distance necessary for two structures with different C values to have the same energy:

$$\left(\frac{(r_1/\sigma_1)_b}{(r_1/\sigma_1)_a}\right)_{E_b=E_a} = \left(\frac{C_b}{C_a}\right)^{(1/n)} \tag{4}$$

in which b and a are two different structures and the subscript $E_b = E_a$ indicates that the energy of the two structures are equal. We can also rewrite eq 4 in terms of ϕ_m:

$$\left(\frac{\phi_{m,b}}{\phi_{m,a}}\right)_{E_b=E_a} = \left(\frac{C_b}{C_a}\right)^{(3/n)} \tag{5}$$

From this, we calculate the minimum ϕ_m that a low C structure can have and still be stable relative to a structure with high C and ϕ_m values. We show this in Figure 7 by comparing the energy for different C and n values to a structure with $C = 12$. The y-axis represents the smallest ϕ_m that a structure with a given C value can have relative to another structure with $C = 12$ and still be stable. In this calculation, we are neglecting any neighbor shells beyond the first one and assuming structures of equal stoichiometry.

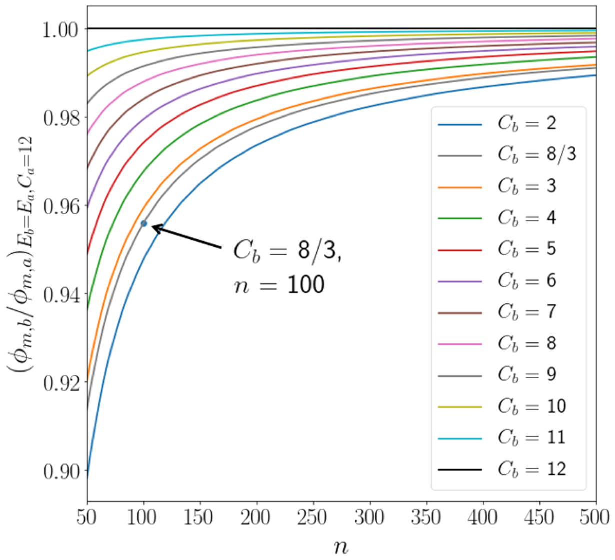

Figure 7. Plots of the lowest packing fraction ϕ_m that a structure *b* with a given number of nearest contacts *C* can have and still be stable relative to another structure *a* with higher *C* and ϕ_m values. In this plot, we define structure *a* as having $C = 12$ in analogy with FCC. The subscript $E_b = E_a$ indicates that the energies of the two structures are equal, so the curves represent lower bounds on what $\phi_{m,b}$ can be for a stable structure. These curves were computed with eq 5. In all cases, we assume that any non-nearest neighbors contribute negligibly to the energy, which is a more accurate approximation at higher *n*.

We see in Figure 7 that a low C value can stabilize many low ϕ_m structures, even when $n > 100$. This is essentially why, in Figure 2, differences exist between $n = 100$ and $n = \infty$. As established earlier, AlB_2 has 8/3 nearest contacts per particle for $\gamma \approx 0.46$; we indicate this point in Figure 7 for $n = 100$. We note that for many structures, including the AlB_2 and $NaZn_{13}$ structures shown, the second shell of neighboring particles is only slightly beyond the first, and thus the approximation in eq 3 is large for smaller n, and the curves shown in Figure 7 should be interpreted qualitatively for real structures.

Low *n* Limit. For $n = 6$, every binary phase becomes unstable with respect to two phase-separated FCC structures containing only large and only small particles, respectively. Although the same observation has been made previously for a smaller group of candidate structures,[23,61] we were surprised to see this occur for our much larger group of candidate structures. Excluding the Laves phases, which are destabilized for all γ only below $n = 7$, every binary structure is destabilized for $n < 13$. This destabilization necessarily results from the energetic cost of neighbor shells beyond the first. Thus, it seems as though FCC has a particularly favorable set of neighbor shells for very soft particles.

As mentioned previously, other work has shown that reducing the additivity between unlike particles results in the observation of more binary phases.[23] We keep our potential additive for consistency with our results at higher n, but, as others have noted,[61,62] it is likely that the assumption of additivity for very soft, repulsive particles is not applicable to many binary self-assembly experiments. For our final optimization run at $n = 6$, we truncate our potential at the fairly long distance of 12σ, which makes it very unlikely that the truncation significantly influenced our results. We also note the previous reports of fluid−fluid phase separation for the IPL model at $\gamma = 1/3$ and $n = 6$.[63] In this paper, our primary focus is on higher values of n.

Experimental Relevance. Here, we discuss a few experimental systems where we believe softly repulsive forces likely play a role in self-assembly: colloids thought to behave like hard spheres ("nearly hard spheres"), certain metal and semiconductor nanoparticles, and like-charged colloids. We explicitly neglect discussing certain cases where we expect our model to fail, such as colloids functionalized with complementary DNA or oppositely charged colloids, who probably have a significantly different driving force for assembly.[64,65] We also discuss why certain phases we predict to be stable have not been observed experimentally and possible implications for the behavior of atomic systems at high pressure.

Our results indicate that softness plays a role in binary colloidal crystals with "nearly hard" colloidal spheres, as their effective n is often less than or around 100.[22] The phases observed thus far in experiments are NaCl, AlB_2, $NaZn_{13}$, and the Laves phases (with various degrees of stacking disorder).[2,24,66] We find that intermediate hardness ($\sim 20 < n < 100$) increases the range of γ over which each of these structures is stable relative to $n = \infty$. Furthermore, we find that some densely packed phases that have not been reported in experiment are destabilized by softness, including d-NaCl, AB_3, and d-AlB_2. We suspect that particle softness may be partially responsible for their failure to assemble in experiment.

Interestingly, all of the experimentally observed phases reported in the literature are also known to be stabilized by entropy in binary hard sphere systems; thus entropy and softness likely both play a role in their formation. Whereas we do not quantify their relative contributions in this study, we can say that increasing the softness of the particles (at least to $n \sim 30$) should increase their likelihood to self-assemble. In fact, a recent report found that repulsive softness did promote the self-assembly of Laves phases, in direct agreement with our predictions.[50] Decreasing the role of entropy in such systems by reducing the temperature or increasing the density should further increase their correspondence with our phase diagram; it would be interesting to see then if the stable phases we find that have not been observed in experiment (*e.g.*, AB, AB_3) could be experimentally realized.

Our results are particularly interesting with regards to the self-assembly of the Laves phases with polymer microgels reported by Schaertl *et al.*[24] The Laves phases are known to be stabilized by entropy at finite temperatures in hard sphere systems—a fact that was used to justify their appearance in these systems. However, Schaertl *et al.* estimated the n and γ values of their particles to be ∼45 and ∼0.77, respectively—only slightly outside of the region in which we predict the Laves phases to be stable due solely to the softness of the interparticle interactions. Thus, we strongly suspect that enthalpic effects played a role in the observation of the Laves phases in that study.[24]

Experiments with metal and semiconductor nanoparticles have yielded several phases in addition to those observed for nearly hard spheres.[3,5,6] We also see two of these additional phases in our phase diagram: AB_4[44] and CaB_6.[46] The appearance of these phases in addition to those observed for nearly hard spheres implies that repulsive forces also play a key role in their assembly. Nonetheless, our results will not account for several of the binary colloidal crystals observed in experiment. These include structures with lower ϕ_m (*e.g.*, AuCu, Li_3Bi, Fe_4C; with our model, structures generally must have a fairly high ϕ_m value to be stable). For many of these nanoparticles, the size of the ligand corona is comparable to that of the nanoparticle core and, accounting for the stability of these structures, has thus far only been accomplished by the orbifold topological model for ligand behavior.[67,68] In predicting some experimentally observed phases but not others, our model may be useful in determining when interactions more complicated than pairwise repulsion are influencing phase behavior.

Fewer reports of the self-assembly of binary structures with like-charged particles exist, but most of the reported structures are similar to those reported for other repulsive particles. The most notable results are those of Hachisu *et al.*,[1,18] who investigated binary suspensions of charged latex particles over 30 years ago. They found every structure observed for nearly hard spheres, as well as two additional ones: $CaCu_5$, which is commonly observed in nanoparticle assembly, and a structure with stoichiometry L_1S_4. Further reports of the structures observed in nearly hard sphere systems have appeared since then;[17,69] our finding that these phases are also stabilized by interaction softness explains their occurrence. Below we discuss the possible reasons why $CaCu_5$ does not appear in our phase diagram, but the few reports of the L_1S_4 structure make its experimental observation harder to understand. Recently, more self-assembly experiments with polydisperse charged particles have been reported,[69] so hopefully future results will clarify certain discrepancies between experiment and our phase diagram.

We also find a few phases to be enthalpically stable for soft particles that have not been reported in experiment. Most notable are AB and AB_3; we find them to be stable for γ values commonly examined in experiment. Our finite temperature results clearly explain the instability of AB_3. We could not rule out the stability of the AB phase on the basis of entropy, but instead suspect its nonappearance is due to kinetic effects. $CaCu_5$ and $NaZn_{13}$ commonly self-assemble in experiment for similar γ values, and previous research has indicated that both of these phases may have particularly low nucleation barriers, which could cause them to form instead of the equilibrium phases.[18,36]

Finally, we note that softness may be an important factor in preventing certain densely packed phases from being observed in atomic systems. Many recently discovered densely packed phases[42,43] appear to not correspond to any known atomic structure. They include phases represented in our phase diagram as d-AlB_2, d-NaCl, AB_3, and a few others produced by the candidate structures listed in Table 2. Our results indicate that a very small amount of interaction softness suffices to destabilize many of these densely packed structures in favor of more commonly observed structures (*e.g.*, the Laves phases, AlB_2), even at the high pressures where densely packed phases are more likely to appear.

CONCLUSIONS

We investigated the influence of interparticle interaction softness on the solid phase behavior of binary sphere systems by determining the ground state enthalpies of a wide variety of structures modeled by an additive inverse power law potential. We found that a surprisingly small amount of softness can influence the phase diagram, and that considerable softness will destabilize every examined binary phase relative to coexisting single-component FCC phases at zero temperature. We compared our results to a long list of experimental findings. We suspect that the softness of colloidal particles is responsible for the lack of observation of certain densest packings in experiment and posit that particle softness likely influences the frequent observation of structures with icosahedral local order.

In this study, we neglected all kinetic influences on the phase behavior, and only investigated entropic effects for a few cases. In doing so, we vastly enlarged the space of structures we were able to examine, as both free energy calculations and crystallization simulations from disordered initial conditions can be computationally expensive. Despite this focus on ground state crystal phases, our work helps explain why certain structures not described by dense packings are observed in experiments on binary colloidal crystals. We expect our findings to be particularly useful for those working with particles of variable softness, such as charged particles, polymer beads, or small nanoparticles functionalized with sterically interacting ligands, and to guide the design of particle interactions to self-assemble target structures, particularly in low temperature or high pressure systems where entropy does not play a significant role.

METHODS

We calculated the ground state phase diagram by computing the enthalpy H of different structures at temperature $T = 0$ and reduced pressure $P\sigma^3/\epsilon = 1$. The well-known scaling properties of the IPL potential model[30,37] allow the calculation of H at any P for a configuration of N particles through a calculation of potential energy at a given number density (see section S1 of the Supporting Information for a derivation).

We found low enthalpy structures using a basin hopping global minimization technique on the free parameters of the Wyckoff sites of particular space groups. For example, we optimized over structures with space group symmetry $C2/m$ (no. 12) with the large particles in Wyckoff site 2*a* and the small particles in Wyckoff site 4*i*. Wyckoff site 4*i* has two free parameters and the monoclinic unit cell of space group $C2/m$ has an additional three parameters that can be optimized (β, where a, b, and c correspond to the lattice vectors of the unit cell and β is the angle between a and c), for a total of 5 degrees of freedom. In structures where we optimized the lattice vectors, we limited b/a and c/a to between 0.25 and 4 if no dense known packings exist outside those bounds. In certain cases where we know dense packings exist outside those bounds, we expanded the upper bound from 4 to 6. For monoclinic structures, we kept θ between 60 and 120°, as every known dense packing is within those bounds. Limiting these parameters reduced errors resulting from finite size effects. Candidate space groups and Wyckoff sites (see Table 2) were selected from those thought to produce structures with high ϕ_m[43,70] or experimentally observed structures. Structures are labeled by their atomic equivalent if known; other structures we found to be stable are labeled by their stoichiometry. In general, the stoichiometry of a phase is determined from the number of particles in large (L) or small (S) Wyckoff sites. We did not include some known dense packing phases because they have exceedingly low symmetry[41,42] and thus would require extensive time to optimize; however, in such cases, we included slightly symmetrized versions of the structures with only marginally reduced ϕ_m (typically ~0.2% less). Our overall approach in optimizing the degrees of freedom of Wyckoff sites is similar to approaches in the literature.[43,45,70]

Optimizing over particular space groups and Wyckoff sites enabled us to search a wide array of possible structures while allowing for simple identification of the resulting low energy structure. First, several of the higher symmetry structures had no free parameters (*e.g.*, NaCl) or had well-known free parameters (AlB_2, CaB_6, $MgZn_2$, $NaZn_{13}$), which made their identification trivial. The values of the free parameters would typically vary slightly for different n and γ, similarly to how they vary for atomic crystals. Second, if the lower symmetry space groups produced structures with the same energy as those of known identity that we also examined, we would conclude, after visual inspection, that they were identical. This situation was extremely common, as several low symmetry space groups reduced to NaCl or AlB_2. Third, if the structure did not correspond to a known higher symmetry structure, we compared their packing fractions and appearance to structures reported to be dense packings in other papers, allowing us to identify AB, AB_2, AB_3, and AB_6. As with the more well-known structures the free parameters of these structures would typically vary slightly with different γ and n. Finally, AB_4 was identified by comparison with a well-described experimental structure.[44] Note that the last two tasks greatly simplified by the fact that most of our candidate space groups were motivated by reports of dense packings and experimental structures.

Using the Python library Scipy's[71] functions for basin hopping[72] and sequential least-squares programming minimization, we conducted global minimization on almost every structure for IPL exponent n between 6 and 100 and γ between 0.3 and 0.9. The exceptions are two structures with a large number of degrees of freedom (specifically the two with space group symmetry *Cm* (no. 8)); they were only optimized for γ in the vicinity of where they are known to produce dense packings ($0.43 \leq \gamma \leq 0.52$).[42] We performed at least two unbiased runs of 200 basin hopping steps for each structure with more than two degrees of freedom. After conducting the unbiased global optimization runs, we determined which structures are most stable for particular values of n and γ, and for those structures we conducted another nine local minimization runs for each n and γ, starting from the values of the free parameters found previously for the state point, as well as those for the eight immediately neighboring n and γ values. The second run had a lower tolerance for convergence and served to refine the boundaries of phase stability. The presence of distinct regions of structural stability in our phase diagram gives us confidence that we accurately detected each enthalpy minimum.

The lowest enthalpy phases in the $n = \infty$ limit correspond to the densest packing phases at a given γ and stoichiometry. With the exception of AB_4 (a dense packing discovered in this project), the putative densest packing phases were taken from the literature. For AB_4 and the approximations of the densely packed phases, we conducted short basin hopping runs to optimize their ϕ_m for particular γ values.

The enthalpy of the candidate structures during optimization was evaluated by constructing a perfect crystal containing many unit cells and evaluating the enthalpy of a single, central unit cell. These perfect structures were all constructed at a number density of $1/\sigma^3$. The number of particles was varied from ~500 to ~100 000, depending on the n used. For the unbiased basin hopping runs, we truncated our potential at distances varying from 4σ to 10σ; for the final nine local optimization runs, we truncated it at distances varying from 6σ to 12σ. Long-range corrections were applied to account for the finite cutoffs of the potential. The signac data management framework supported our computational workflow and data management.[73,74]

The free energies of particular phases at finite temperature were calculated using the Einstein molecule method with the HOOMD-blue simulation toolkit.[75,76] The Einstein molecule method is a variant

DOI: 10.1021/acsnano.9b04274

of the Frenkel−Ladd method in which the position of a single particle within the simulation box is constrained instead of the center of mass.[54] The methods involve using thermodynamic integration to compute the free energy differences between a crystal of harmonic oscillators to the real crystal under scrutiny; the accuracy of the method is limited only by numerical precision. Further details of the method have been reported in several places.[55,54,77] We set the de Broglie wavelength of each particle equal to unity; doing so does not affect phase equilibrium. The integration was performed in 20 steps using an Einstein molecule with a harmonic constant of $2 \times 10^5\ \epsilon/\sigma^2$. To reduce the errors from using a large harmonic constant, we used a time step of $10^{-4}\ \sigma(m/kT)^{1/2}$.

Einstein molecule calculations were performed at constant density and $kT/\epsilon = 1$ on crystals of at least 1000 particles. The density was chosen to be close to the melting point, and the temperature was maintained with the Langevin thermostat. Pressure−volume data were obtained from conducting NPT simulations with the Nosé-Hoover thermostat and barostat; these data were thermodynamically integrated to find G at a particular pressure. The pressure presented in Table 1 was chosen to be slightly lower than the melting point of $\mathrm{FCC_S}$ (as determined by interpolating the data of Agrawal *et al.*[55]) but high enough for the crystal to be metastable. Standard deviations were computed by running three independent replicas of every simulation.

ASSOCIATED CONTENT

Ⓢ Supporting Information

The Supporting Information is available free of charge on the ACS Publications website at DOI: 10.1021/acsnano.9b04274.

> Derivation of equations used to calculate enthalpy; review of IPL and hard sphere thermodynamic scaling parameters; unit cell parameters and visualizations of unusual stable structures (PDF)

AUTHOR INFORMATION

Corresponding Author

*E-mail: sglotzer@umich.edu.

ORCID

R. Allen LaCour: 0000-0002-0572-2286
Julia Dshemuchadse: 0000-0003-2310-6687
Sharon C. Glotzer: 0000-0002-7197-0085

Notes

The authors declare no competing financial interest.

ACKNOWLEDGMENTS

This research was supported in part by the National Science Foundation, Division of Materials Research Award No. DMR 1409620. Development and application of signac for use in this work was supported by MICCoM, as part of the Computational Materials Sciences Program funded by the U.S. Department of Energy, Office of Science, Basic Energy Sciences, Materials Sciences and Engineering Division through Argonne National Laboratory, under contract number DE-AC02-06CH11357. Computational resources and services were supported by Advanced Research Computing at the University of Michigan, Ann Arbor.

REFERENCES

(1) Hachisu, S.; Yoshimura, S. Optical Demonstration of Crystalline Superstructures in Binary Mixtures of Latex Globules. *Nature* **1980**, *283*, 188.

(2) Bartlett, P.; Ottewill, R.; Pusey, P. N. Superlattice Formation in Binary Mixtures of Hard Sphere Colloids. *Phys. Rev. Lett.* **1992**, *68*, 3801−3804.

(3) Shevchenko, E. V.; Talapin, D. V.; Kotov, N. A.; O'Brien, S.; Murray, C. B. Structural Diversity in Binary Nanoparticle Superlattices. *Nature* **2006**, *439*, 55−59.

(4) Evers, W. H.; Nijs, B. D.; Filion, L.; Castillo, S.; Dijkstra, M.; Vanmaekelbergh, D. Entropy-Driven Formation of Binary Semiconductor-Nanocrystal Superlattices. *Nano Lett.* **2010**, *10*, 4235−4241.

(5) Ye, X.; Zhu, C.; Ercius, P.; Raja, S. N.; He, B.; Jones, M. R.; Hauwiller, M. R.; Liu, Y.; Xu, T.; Alivisatos, A. P. Structural Diversity in Binary Superlattices Self-Assembled from Polymer-Grafted Nanocrystals. *Nat. Commun.* **2015**, *6*, 10052.

(6) Boles, M. A.; Talapin, D. V. Many-Body Effects in Nanocrystal Superlattices: Departure from Sphere Packing Explains Stability of Binary Phases. *J. Am. Chem. Soc.* **2015**, *137*, 4494−4502.

(7) Talapin, D. V.; Lee, J. S.; Kovalenko, M. V.; Shevchenko, E. V. Prospects of Colloidal Nanocrystals for Electronic and Optoelectronic Applications. *Chem. Rev.* **2010**, *110*, 389−458.

(8) Ye, X.; Chen, J.; Diroll, B. T.; Murray, C. B. Tunable Plasmonic Coupling in Self- Assembled Binary Nanocrystal Superlattices Studied by Correlated Optical Microspectrophotometry and Electron Microscopy. *Nano Lett.* **2013**, *13*, 1291−1297.

(9) Kang, Y.; Ye, X.; Chen, J.; Qi, L.; Diaz, R. E.; Doan-Nguyen, V.; Xing, G.; Kagan, C. R.; Li, J.; Gorte, R. J.; Stach, E. A.; Murray, C. B. Engineering Catalytic Contacts and Thermal Stability: Gold/Iron Oxide Binary Nanocrystal Superlattices for CO Oxidation. *J. Am. Chem. Soc.* **2013**, *135*, 1499−1505.

(10) Chen, J.; Ye, X.; Oh, S. J.; Kikkawa, J. M.; Kagan, C. R.; Murray, C. B. Bistable Magnetoresistance Switching in Exchange-Coupled CoFe2O4−Fe3O4 Binary Nanocrystal Superlattices by Self-Assembly and Thermal Annealing. *ACS Nano* **2013**, *7*, 1478−1486.

(11) Boles, M. A.; Engel, M.; Talapin, D. V. Self-Assembly of Colloidal Nanocrystals: From Intricate Structures to Functional Materials. *Chem. Rev.* **2016**, *116*, 11220−11289.

(12) Murray, M. J.; Sanders, J. V. Close-Packed Structures of Spheres of Two Different Sizes II. The Packing Densities of Likely Arrangements. *Philos. Mag. A* **1980**, *42*, 721−740.

(13) Chen, Z.; Moore, J.; Radtke, G.; Sirringhaus, H.; O'Brien, S. Binary Nanoparticle Superlattices in the Semiconductor-Semiconductor System: CdTe and CdSe. *J. Am. Chem. Soc.* **2007**, *129*, 15702−15709.

(14) Ye, X.; Chen, J.; Engel, M.; Millan, J. A.; Li, W.; Qi, L.; Xing, G.; Collins, J. E.; Kagan, C. R.; Li, J.; Glotzer, S. C.; Murray, C. B. Competition of Shape and Interaction Patchiness for Self-Assembling Nanoplates. *Nat. Chem.* **2013**, *5*, 466.

(15) Schultz, B. A.; Damasceno, P. F.; Engel, M.; Glotzer, S. C. Symmetry Considerations for the Targeted Assembly of Entropically Stabilized Colloidal Crystals *via* Voronoi Particles. *ACS Nano* **2015**, *9*, 2336−2344.

(16) Torquato, S. Perspective: Basic Understanding of Condensed Phases of Matter *via* Pack- ing Models. *J. Chem. Phys.* **2018**, *149*, 020901.

(17) Lorenz, N. J.; Schope, J. H.; Reiber, H.; Palberg, T.; Wette, P.; Klassen, I.; Holland- Moritz, D.; Herlach, D.; Okubo, T. Phase Behaviour of Deionized Binary Mixtures of Charged Colloidal Spheres. *J. Phys.: Condens. Matter* **2009**, *21*, 464116.

(18) Yoshimura, S.; Hachisu, S. Order Formation in Binary Mixtures of Monodisperse Latices. *Prog. Colloid Polym. Sci.* **1983**, *68*, 59−70.

(19) Kaushik, A. P.; Clancy, P. Solvent-Driven Symmetry of Self-Assembled Nanocrystal Superlattices - A Computational Study. *J. Comput. Chem.* **2013**, *34*, 523−532.

(20) Cersonsky, R. K.; van Anders, G.; Dodd, P. M.; Glotzer, S. C. Relevance of Packing to Colloidal Self-Assembly. *Proc. Natl. Acad. Sci. U. S. A.* **2018**, *115*, 1439−1444.

(21) Bryant, G.; Williams, S. R.; Qian, L.; Snook, I. K.; Perez, E.; Pincet, F. How Hard is a Colloidal "Hard-Sphere" Interaction? *Phys. Rev. E: Stat. Phys., Plasmas, Fluids, Relat. Interdiscip. Top.* **2002**, *66*, 060501.

(22) Royall, C. P.; Poon, W. C. K.; Weeks, E. R. In Search of Colloidal Hard Spheres. *Soft Matter* **2013**, *9*, 17−27.

(23) Travesset, A. Binary Nanoparticle Superlattices of Soft-Particle Systems. *Proc. Natl. Acad. Sci. U. S. A.* **2015**, *112*, 9563−9567.

(24) Schaertl, N.; Botin, D.; Palberg, T.; Bartsch, E. Formation of Laves phases in Buoyancy Matched Hard Sphere Suspensions. *Soft Matter* **2018**, *14*, 5130−5139.

(25) Eldridge, M. D.; Madden, P. A.; Frenkel, D. Entropy-Driven Formation of a Superlattice in a Hard-Sphere Binary Mixture. *Nature* **1993**, *365*, 35−37.

(26) Frenkel, D. Entropy-Driven Phase Transitions. *Phys. A* **1999**, *263*, 26−38.

(27) Dijkstra, M.; van Roij, R.; Evans, R. Phase Diagram of Highly Asymmetric Binary Hard-Sphere Mixtures. *Phys. Rev. E: Stat. Phys., Plasmas, Fluids, Relat. Interdiscip. Top.* **1999**, *59*, 5744−5771.

(28) Hynninen, A. P.; Filion, L.; Dijkstra, M. Stability of LS and L S2 Crystal Structures in Binary Mixtures of Hard and Charged Spheres. *J. Chem. Phys.* **2009**, *131*, No. 064902.

(29) Damasceno, P. F.; Engel, M.; Glotzer, S. C. Predictive Self-Assembly of Polyhedra into Complex Structures. *Science* **2012**, *337*, 453−457.

(30) Hoover, W. G.; Ross, M.; Johnson, K. W.; Henderson, D.; Barker, J. A.; Brown, B. C. Soft Sphere Equation of State. *J. Chem. Phys.* **1970**, *52*, 4931−4941.

(31) Hansen, J.; Schiff, D. Influence of Interatomic Repulsion on the Structure of Liquids at Melting. *Mol. Phys.* **1973**, *25*, 1281−1290.

(32) Horst, N.; Travesset, A. Prediction of Binary Nanoparticle Superlattices from Soft Potentials. *J. Chem. Phys.* **2016**, *144*, No. 014502.

(33) O'Toole, P. I.; Hudson, T. S. New High-Density Packings of Similarly Sized Binary Spheres. *J. Phys. Chem. C* **2011**, *115*, 19037−19040.

(34) Eldridge, M. D.; Madden, P. A.; Pusey, P. N.; Bartlett, P. Binary Hard-Sphere Mixtures: A Comparison Between Computer Simulation and Experiment. *Mol. Phys.* **1995**, *84*, 395−420.

(35) Hynninen, A. P.; Thijssen, J. H.; Vermolen, E. C.; Dijkstra, M.; Van Blaaderen, A. Self-Assembly Route for Photonic Crystals with a Bandgap in the Visible Region. *Nat. Mater.* **2007**, *6*, 202−205.

(36) Bodnarchuk, M. I.; Kovalenko, M. V.; Heiss, W.; Talapin, D. V. Energetic and Entropic Contributions to Self-Assembly of Binary Nanocrystal Superlattices: Temperature as the Structure-Directing Factor. *J. Am. Chem. Soc.* **2010**, *132*, 11967−11977.

(37) Travesset, A. Phase Diagram of Power Law and Lennard-Jones Systems: Crystal Phases. *J. Chem. Phys.* **2014**, *141*, 164501.

(38) Schneider, J.; Wiemann, M.; Rabe, A.; Bartsch, E. On Tuning Microgel Character and Softness of Cross-Linked Polystyrene Particles. *Soft Matter* **2017**, *13*, 445−457.

(39) Silvera Batista, C. A.; Larson, R. G.; Kotov, N. A. Nonadditivity of Nanoparticle Interactions. *Science* **2015**, *350*, 1242477.

(40) Bergerhoff, G.; Hundt, R.; Sievers, R.; Brown, I. D. The Inorganic Crystal Structure Data Base. *J. Chem. Inf. Model.* **1983**, *23*, 66−69.

(41) Hopkins, A. B.; Jiao, Y.; Stillinger, F. H.; Torquato, S. Phase Diagram and Structural Diversity of the Densest Binary Sphere Packings. *Phys. Rev. Lett.* **2011**, *107*, 125501.

(42) Hopkins, A. B.; Stillinger, F. H.; Torquato, S. Densest Binary Sphere Packings. *Phys. Rev. E* **2012**, *85*, No. 021130.

(43) Filion, L.; Dijkstra, M. Prediction of Binary Hard-Sphere Crystal Structures. *Phys. Rev. E* **2009**, *79*, 46714.

(44) Talapin, D. V.; Shevchenko, E. V.; Bodnarchuk, M. I.; Ye, X.; Chen, J.; Murray, C. B. Quasicrystalline Order in Self-Assembled Binary Nanoparticle Superlattices. *Nature* **2009**, *461*, 964−967.

(45) Kummerfeld, J. K.; Hudson, T. S.; Harrowell, P. The Densest Packing of AB Binary Hard-Sphere Homogeneous Compounds Across all Size Ratios. *J. Phys. Chem. B* **2008**, *112*, 10773−10776.

(46) Ye, X.; Chen, J.; Murray, C. B. Polymorphism in Self-Assembled AB6 Binary Nanocrystal Superlattices. *J. Am. Chem. Soc.* **2011**, *133*, 2613−2620.

(47) Ganagalla, S. R.; Punnathanam, S. N. Free Energy Barriers for Homogeneous Crystal Nucleation in a Eutectic System of Binary Hard Spheres. *J. Chem. Phys.* **2013**, *138*, 174503.

(48) Bommineni, P. K.; Punnathanam, S. N. Molecular Simulation of Homogeneous Crystal Nucleation of AB2 Solid Phase from a Binary Hard Sphere Mixture. *J. Chem. Phys.* **2017**, *147*, No. 064504.

(49) Bommineni, P. K.; Varela-Rosales, N. R.; Klement, M.; Engel, M. Complex Crystals from Size-Disperse Spheres. *Phys. Rev. Lett.* **2019**, *122*, 128005.

(50) Dasgupta, T.; Coli, G. M.; Dijkstra, M. Softness Suppresses Fivefold Symmetry and Enhances Crystallization of Binary Laves Phases in Nearly Hard Spheres. *arXiv1906.1068* **2019**; https://arxiv.org/abs/1906.10680 (last accessed on 10/1/2019).

(51) Prestipino, S.; Saija, F.; Giaquinta, P. V. Phase Diagram of Softly Repulsive Systems: The Gaussian and Inverse-Power-Law Potentials. *J. Chem. Phys.* **2005**, *123*, 144110.

(52) Robbins, M. O.; Kremer, K.; Grest, G. S. Phase Diagram and Dynamics of Yukawa Systems. *J. Chem. Phys.* **1988**, *88*, 3286−3312.

(53) Frenkel, D.; Ladd, A. J. C. New Monte Carlo Method to Compute the Free Energy of Arbitrary Solids. Application to the Fcc and Hcp Phases of Hard Spheres. *J. Chem. Phys.* **1984**, *81*, 3188−3193.

(54) Vega, C.; Noya, E. G. Revisiting the Frenkel-Ladd Method to Compute the Free Energy of Solids: The Einstein Molecule Approach. *J. Chem. Phys.* **2007**, *127*, 154114.

(55) Agrawal, R.; Kofke, D. A. Thermodynamic and Structural Properties of Model Systems at Solid-Fluid Coexistence. *Mol. Phys.* **1995**, *85*, 23−42.

(56) Melnyk, T. W.; Knop, O.; Smith, W. R. Extremal Arrangements of Points and Unit Charges on a Sphere: Equilibrium Configurations Revisited. *Can. J. Chem.* **1977**, *55*, 1745−1761.

(57) Clare, B. W.; Kepert, D. L. The Closest Packing of Equal Circles on a Sphere. *Proc. R. Soc. London, Ser. A* **1986**, *405*, 329−344.

(58) Travesset, A. Nanoparticle Superlattices as Quasi-Frank-Kasper Phases. *Phys. Rev. Lett.* **2017**, *119*, 115701.

(59) Heyes, D. M.; Brańka, A. C. The Influence of Potential Softness on the Transport Coef- ficients of Simple Fluids. *J. Chem. Phys.* **2005**, *122*, 234504.

(60) Lange, E.; Caballero, J. B.; Puertas, A. M.; Fuchs, M. Comparison of Structure and Transport Properties of Concentrated Hard and Soft Sphere Fluids. *J. Chem. Phys.* **2009**, *130*, 174903.

(61) Finlayson, S. D.; Bartlett, P. Non-Additivity of Pair Interactions in Charged Colloids. *J. Chem. Phys.* **2016**, *145*, 034905.

(62) Herlach, D. M.; Palberg, T.; Klassen, I.; Klein, S.; Kobold, R. Overview: Experimental Studies of Crystal Nucleation: Metals and Colloids. *J. Chem. Phys.* **2016**, *145*, 211703.

(63) Kerley, G. I. Equations of State and Gas-−Gas Separation in Soft-Sphere Mixtures. *J. Chem. Phys.* **1989**, *91*, 1204−1210.

(64) Macfarlane, R. J.; Lee, B.; Jones, M. R.; Harris, N.; Schatz, G. C.; Mirkin, C. A. Nanoparticle Superlattice Engineering with DNA. *Science* **2011**, *334*, 204−208.

(65) Vo, T.; Venkatasubramanian, V.; Kumar, S.; Srinivasan, B.; Pal, S.; Zhang, Y.; Gang, O. Stoichiometric Control of DNA-Grafted Colloid Self-Assembly. *Proc. Natl. Acad. Sci. U. S. A.* **2015**, *112*, 4982−4987.

(66) Hunt, N.; Jardine, R.; Bartlett, P. Superlattice Formation in Mixtures of Hard-Sphere Colloids. *Phys. Rev. E: Stat. Phys., Plasmas, Fluids, Relat. Interdiscip. Top.* **2000**, *62*, 900−913.

(67) Travesset, A. Topological Structure Prediction in Binary Nanoparticle Superlattices. *Soft Matter* **2017**, *13*, 147−157.

(68) Travesset, A. Soft Skyrmions, Spontaneous Valence and Selection Rules in Nanoparticle Superlattices. *ACS Nano* **2017**, *11*, 5375−5382.

(69) Cabane, B.; Li, J.; Artzner, F.; Botet, R.; Labbez, C.; Bareigts, G.; Sztucki, M.; Goehring, L. Hiding in Plain View: Colloidal Self-Assembly from Polydisperse Popu- lations. *Phys. Rev. Lett.* **2016**, *116*, 208001.

(70) Hudson, T. S; Harrowell, P. Structural Searches Using Isopointal Sets as Generators: Densest Packings for Binary Hard Sphere Mixtures. *J. Phys.: Condens. Matter* **2011**, *23*, 194103.

(71) Jones, E.; Oliphant, T.; et al. Scipy: Open Source Scientific Tools for Python. 2001; http://www.scipy.org/ (last accessed on 12/1/18).

(72) Wales, D. J.; Doye, J. P. K. Global Optimization by Basin-Hopping and the Lowest Energy Structures of Lennard-Jones Clusters Containing up to 110 Atoms. *J. Phys. Chem. A* **1997**, *101*, 5111−5116.

(73) Adorf, C. S.; Ramasubramani, V.; Dice, B. D.; Henry, M. M.; Dodd, P. M.; Glotzer, S. C. glotzerlab/signac. 2019; https://zenodo.org/record/2581327/export/schemaorg_jsonld#.XcRA5DNKiUk (accessed on 09/05/2019).

(74) Adorf, C. S.; Dodd, P. M.; Ramasubramani, V.; Glotzer, S. C. Simple Data and Workflow Management with the signac Framework. *Comput. Mater. Sci.* **2018**, *146*, 220−229.

(75) Anderson, J. A.; Lorenz, C. D.; Travesset, A. General Purpose Molecular Dynamics Simulations Fully Implemented on Graphics Processing Units. *J. Comput. Phys.* **2008**, *227*, 5342−5359.

(76) Glaser, J.; Nguyen, T. D.; Anderson, J. A.; Lui, P.; Spiga, F.; Millan, J. A.; Morse, D. C.; Glotzer, S. C. Strong Scaling of General-Purpose Molecular Dynamics Simulations on GPUs. *Comput. Phys. Commun.* **2015**, *192*, 97−107.

(77) Vega, C.; Sanz, E.; Abascal, J. L. F.; Noya, E. G. Determination of Phase Diagrams *via* Computer Simulation: Methodology and Applications to Water, Electrolytes and Proteins. *J. Phys.: Condens. Matter* **2008**, *20*, 153101.

DOI: 10.1021/acsnano.9b04274
ACS Nano XXXX, XXX, XXX−XXX